RSC Advances

ROYAL SOCIETY OF CHEMISTRY

www.rsc.org/advances

RSC Advances

RSCPublishing

ARTICLE

Cite this: DOI: 10.1039/x0xx00000x

Received 00th xxxx 2015,

Accepted 00th xxxx 2015

DOI: 10.1039/x0xx00000x

www.rsc.org/

One-step and template-free preparation of hierarchical porous carbons with high capacitive performance

Jin Zhou*, Zhongshen Zhang, Zhaohui Li, Tingting Zhu, and Shuping Zhuo*

Considering the wide application of hierarchical porous carbon materials (HPCs), one-step and template-free preparation of HPCs is much attractive. In this work, HPCs are prepared by direct carbonization of phenolic resin carboxylic salt xerogels. The morphology and porosity of the prepared carbon materials are characterized by scanning electron microscopy, transmission electron microscopy and nitrogen adsorption/desorption. The obtained HPCs possesses typically hierarchical porosity combined interconnected mesopores and highly accessible micropores with short diffusion length. Due to its unique hierarchical pore texture, the prepared carbon materials shows superior capacitive performance with high specific capacitance, excellent rate capability, and good long-term cycle stability in both KOH and $N(C_2H_5)_4BF_4$/acetonitrile electrolyte. Remarkable energy densities of 29.1 and 6.1 Wh kg^{-1} are delivered by HPC-9d in organic and KOH electrolyte, respectively. At a very high power density of 10 000 W kg^{-1}, the energy densities of HPC-9d still reach up to 14.4 and 4.5 Wh kg^{-1} in organic electrolyte and KOH electrolyte, respectively, suggesting the prepared HPCs possess both high energy density and high power density.

Introduction

Recently, supercapacitors have been attracting significant research interest because this energy storage device shows lots of distinctive merits like high power density, good reversibility, long-term cycle life, and broad energy storage application prospects[1-3]. It is a well-known fact that the capacitive behavior of supercapacitors depends intimately on the physical and chemical properties of their electrode materials, so a great deal of efforts have been put into developing desired electrode materials for supercapacitors[4-9]. Up to now, carbon materials are considered to be one of the most promising electrode materials owing to their advantages of rich in resource, low cost, excellent conductivity, tailored porosity, and quite stable physicochemical properties[10-15].

Carbon materials store electric energies mainly by the electrostatic double-layer uptake at the electrolyte/electrode interfacial regions. The specific surface areas and pore size distributions (PSDs) are the most important factors which affect the capacitive performance of carbon materials. According to the theory by Gogotsi et al. [16-18], the solvation shell of electrolyte ions may be partially removed in micropores, the distance between pore wall and the center of the ion (d) decreases, and then results in a high capacitance according to the equation of $C=\varepsilon A/d$, where A is the surface area, d is the separation between carbon and ions, and ε is the local dielectric constant of the electrolyte. It is clear that, for a high capacitance (energy density), micropores of the carbon electrodes are proved to be optimal. However, for pulse power applications (power density), larger pores are beneficial. There have been many literatures reported that the necessity of mesopores for supercapacitor with high rate performance because these mesopores could promote the mass transport in an electrochemical process[19-22].

To improve both the energy and power characteristics, the advantage of different-level pores should be effectively concerted. So hierarchical porous carbons (HPCs) which simultaneously possess multimodal PSDs of micro-, meso-, and/or macropores are proposed as promising candidate as electrode materials in supercapacitor[20, 23-30]. It is believed that mesopores or macropores with larger pore size could serve as micro reservoirs of electrolyte and the expressway for ion-transport, resulting in a decreased diffusion distance and high power output; meanwhile the micropores within the wall of the meso/macro pores afford high effective surface area for forming electric double layer to obtain a high capacitance. The synergetic effect of multimodal pores imparted the carbon materials with good combination of energy and power density.

So far, templating methods are still most commonly used to design and fabricate HPCs, including hard templating (e.g. porous silica oxide, metal oxide or silica colloid)[20, 26, 28, 29, 31-35] and soft templating methods (e. g. triblock copolymer F127 or ionic liquid) [25, 36-39]. Templating methods are general and versatile to design macropore and mesopore systems, rather than micropore system. Therefore, to obtain a high surface area, a further activation is usually needed to introduce numerous micropores into the carbon skeleton. Apparently, there are some disadvantages, such as complicated preparation technology, relative expensive templates, and rigorous activation process, which limits wide application of HPCs. Based on the above reasons, one-step and template-free synthesis of HPCs is very attractive.

In this work, we report a one-step and template-free method for preparing HPCs by direct carbonization of phenolic resin carboxylic salt xerogels. The process is facile and very easy to handle, and the final HPCs possess typical hierarchical porosity with rational mesopores and numerous short micropores. Their surface area could be up to 1549 m^2 g^{-1}. Such unique structural features endow the prepared HPCs with good capacitive behaviour, high capacitance and excellent rate capability both in organic and aqueous electrolyte.

Experimental

Materials Preparation

Resin hydrogels were prepared by the aqueous polycondensation of 2, 4-dihydroxy benzoic acid with formaldehyde using KOH as a catalyst. In a typical of synthesis, 0.50 g of 2, 4-dihydroxy benzoic acid (3.2 mmol) and 0.18 g of KOH (3.2 mmol) were dissolved in 8.0 g water under magnetic stirring at room temperature, to form a pale yellow clear solution. Afterward, 0.53 g of formalin (37 wt %, 6.5 mmol) was added to the above solution and stirred for ca. 10 min at 25 °C. The solution was then sealed and transferred into an oven at 80 °C. It quickly turned red and solidified within 10 min, and further reacted for 4 h. After drying at 80°C for 24h, the hydrogels were converted into xerogels, and were carbonized in a tubular furnace at a certain temperature (heating rate: 3 °C min^{-1}) under N_2 flow (100 cm^3 min^{-1}) for 2 hours. Finally, the carbon materials were liberated by washing with deionized water till neutral. For convenience, the prepared carbons were denoted as HPC-*x*, where HPC stands for the hierarchical porous carbon, and *x* designates one hundredth of carbonization temperature (in °C). The synthesis route of HPC-9h, HPC-9d and HPC-9t is all the same except for using half, double and triple KOH dosage, respectively. For the preparation of MPC-9, the resin hydrogels are pre-ageing by a hydrothermal treatment at 160 °C for 24h before carbonization. A CMK-3 carbon was prepared through a two-step nanocasting method by using SBA-15 as template according to a previous literature[40].

Materials Characterizations

The morphology and porosity of the prepared carbon materials were observed with a scanning electron microscope (SEM, Sirion 200 FEI Netherlands) and a transmission electron microscope (TEM, JEM2100, JEOL, Japan). Chemical composition was determined by energy dispersive spectroscopy (EDS) measurements (EDS, INCA Energy spectrometer). X-ray diffraction (XRD) patterns were conducted using Brucker D8 Advance diffraction with Cu Ka radiation. Raman spectra were obtained from a LabRAM HR800 from JY Horiba. Nitrogen sorption measurements were performed at -196 °C using ASAP 2020 system (Micrometitics, USA). The carbon materials were degassed at 350 °C overnight before sorption measurements. Brunaner-Emmett-Teller (BET) surface area (S_{BET}) was calculated using the N_2 adsorption isotherm data within the relative pressure of 0.05-0.25. Total pore volume (V_T) was obtained at p/p_0=0.995. Total microspore volume (V_{micro}) was determined by t-plot method. Mesopore volume (V_{meso}) was calculated by subtracting the micropore volume from the total pore volume. PSDs were determined by applying the nonlocal density functional theory (NLDFT) model on the adsorption isotherms and assuming a slit-shape pore. The packing density is determined by a self-designed method. In detail, certain weights of carbon materials are added into a graduated cylinder, compacted and determined the volume. Then, the packing density of carbon materials are calculated by dividing the weight by the volume.

Electrochemical measurement

The working electrodes are prepared by mixing 95 wt% carbon materials and 5 wt% PTFE binders, pressing the mixture onto nickel foam at 15 MPa, and then drying at 120 °C for 10 h. The mass of the active materials loaded on the electrode is 5.0 mg for each electrode. The electrochemical measurements, including cyclic voltammetry (CV), galvanostatic charge/discharge test and electrochemical impedance spectroscopy (EIS), are carried on a CHI660D electrochemical testing station (Chenhua Instruments Co. Ltd., Shanghai). The model capacitors were assembled in a glove box filled with argon (Mikrouna Universal 2440/750, H_2O and O_2<1 ppm) by facing two electrodes sandwiched with a fiber separator when using 1 M tetraethylammonium tetrafluoroborate in acetonitrile ($TEABF_4$/AN) as electrolyte.

The galvanostatic charge/discharge test was performed in a two-electrode system to determine the specific capacitance at current densities in the range of 0.2-50 A g^{-1} and 0.2-20 A g^{-1} for 6 M KOH and 1 M $TEABF_4$/AN electrolyte, respectively. EIS test was performed with alternate current amplitude of 5 mV in KOH electrolyte using a three-electrode system with a platinum plate electrode and a saturated calomel electrode (SCE) as the counter and reference electrode, respectively. The long-term galvanostatic charge/discharge experiments were carried out on an automatic galvanostatic charge/discharge unit (Land CT 2001A, Wuhan, China) at a current density of 2 A g^{-1}.

The specific capacitance is calculated by the following equation:

$$C_m = \frac{4I \times t}{\Delta V \times m} \quad (1)$$

where C_m (F g^{-1}) is the gravimetric specific capacitance of the carbon samples, I (A) is the discharge current, t (s) is the discharge time, ΔV (V) is the potential window of the cell, and m (g) is the total mass of active materials in the cell. The volumetric capacitances are determined by dividing the gravimetric specific capacitance by the packing density of carbon materials.

Energy density (E) and powder density (P) could be calculated from the galvanostatic charge/discharge test using the equations of

$$E = \frac{1}{8} \times C_m \times V^2 \quad (2)$$

$$P = \frac{E}{t} \quad (3)$$

where the C_m, V and t are the gravimetric specific capacitance of the carbon materials, discharge voltage decrease and discharge time, respectively.

Results and discussion

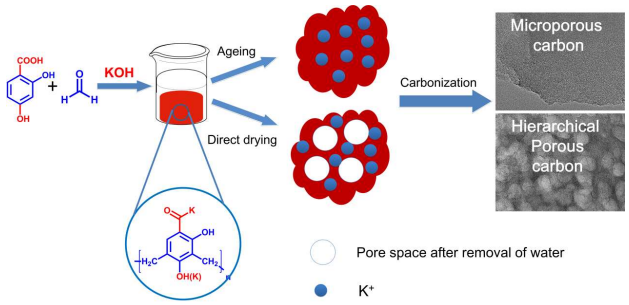

Fig. 1 – Illustration for the synthesis of hierarchical porous carbon materials

Fig. 1 shows the synthesis route of the investigated carbon materials. Firstly, orange resin hydrogels are prepared by the aqueous polycondensation of 2, 4-dihydroxy benzoic acid and formaldehyde using KOH as catalyst. The obtained hydrogels are treated by two methods, one is direct dry at 80 °C, and the other is hydrothermal ageing at 160 °C for 24h before drying (Fig. S1). The HPC-*x* samples are prepared by carbonizing the direct-dried xerogels under N_2 flow in a tubular furnace. Meanwhile, an ultramicroporous carbon material denoted as MPC-9 is prepared by carbonization of the hydrothermal-treated xerogels.

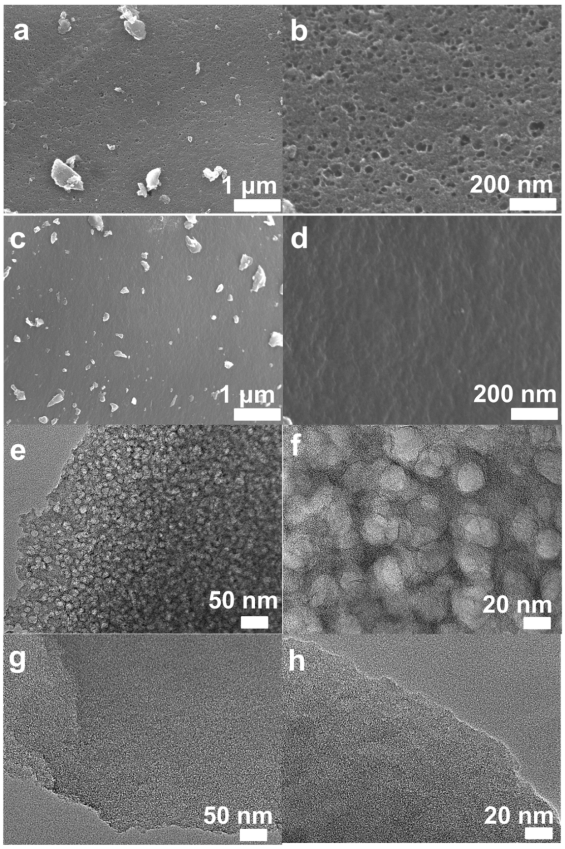

Fig. 2- SEM images of (a, b) HPC-9d and (c, d) MPC-9, and TEM images of (e, f) HPC-9d and (g, h) MPC-9

The morphology and pore texture of the prepared carbon materials are firstly studied by SEM and TEM techniques (Fig. 2, S2 and S3). Under low resolution of SEM observations, the prepared carbon materials looks composed of large carbon blocks (Fig. S2). Lots of rounded pores in the size of dozens of nanometers are observed on the carbon surface of HPC-*x* (Fig. 2b, S2). Comparatively, relative smooth surface is observed for MPC-9, and no clear pores are found, indicating the poor mesoporosity of this carbon. As revealed by TEM images, the HPC-*x* materials have a well-developed pore system consisting of disordered, interconnected and roughly spherical pores mainly in the range of 20–40 nm (Fig. 2, S3). High resolution TEM (HRTEM) images clearly exhibit worm-like micropores on the mesopore walls of HPC-*x*. Notably, the thickness of the mesopore wall is only about a few tens of nanometers, and that is, the length of micropores may be very short. The mesopores stemmed considerably from the hydrogel structures and the potassium ions (K^+) mono-dispersed in phenolic resin hydrogels as a form of $-COO^-K^+$ help to develop highly uniform and interconnected micropores with short channel length on the mesopore walls. Thus, carbon materials with a typical hierarchical porosity are obtained. This kind of hierarchical pore structure was very important to improve the rate capability and large current charge/discharge performance, because the interconnected mesopores can facilitate better mass diffusion and transport, and the micropores could supply efficient pore space to store static charge. Microporous nature of MPC-9 is also proved by HRTEM images (Fig. 2g, h), indicating that the hydrothermal ageing process results in the collapse of the hydrogel structure which is also deduced by the shrinkage of hydrogels after hydrothermal ageing. A well-developed graphite-like structure is observed for HPC-10 (Fig. S3f), which will be discussed hereinbelow. In order to confirm the chemical composition of HPC-x, energy dispersive spectroscopy (EDS) measurements are conducted. Only C and O elements are observed. The O content of HPC-*x* decreases as the activation temperature increases, and is determined to be 5.3-10.5 wt%, respectively. The O content of HPC-9d (8.5%) is higher than that of HPC-9 (7.3%).

Table 1 Texture properties of samples

Sample	S_{BET} ($m^2\ g^{-1}$)	V_T ($cm^3\ g^{-1}$)	V_{meso} ($cm^3\ g^{-1}$)	V_{micro} ($cm^3\ g^{-1}$)	$V_{<1.5\ nm}$ ($cm^3\ g^{-1}$)	$V_{<0.7\ nm}$ ($cm^3\ g^{-1}$)
MPC-9	648	0.33	0	0.33	0.28	0.25
HPC-6	524	0.31	0.06	0.25	0.22	0.21
HPC-7	637	0.37	0.06	0.31	0.26	0.23
HPC-8	803	0.46	0.08	0.38	0.32	0.24
HPC-9	1007	0.62	0.16	0.46	0.37	0.24
HPC-9d	1549	0.81	0.17	0.61	0.48	0.25
HPC-10	966	0.57	0.14	0.43	0.35	0.25

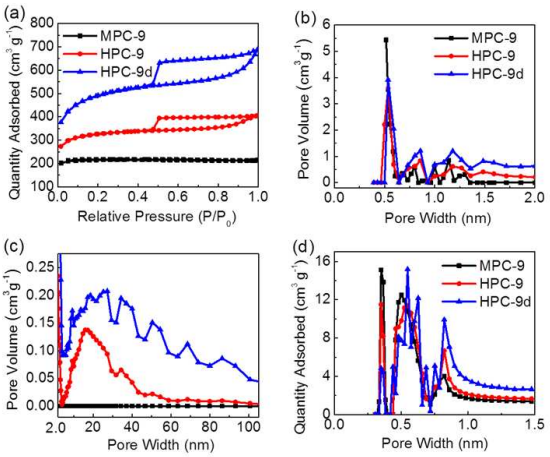

Fig. 3 - (a) N_2 sorption isotherms, (b, c) NLDFT pore size distribution calculated from N_2 adsorption isotherms, (d) NLDFT micropore size distribution calculated from CO_2 adsorpiton isotherms

N_2 sorption measurements are further performed to determine the specific surface area and PSDs of HPC-*x* and MPC-9 (Fig. 3, S4 and Table 1). It could be seen that all the HPC-*x* samples exhibit an isotherm combined type I and IV isotherms. They presented a large nitrogen sorption capacity at relative pressures P/P_0 lower than 0.01, indicating the existence of a well-developed narrow microporosity. They also presented a broad hysteresis loop in a wide relative pressure range from 0.4-1.0, assigned to capillary condensation in mesopores up to tens of nanometers. Stating point of the sorption isotherm for HPC-*x* roughly increases with the increasing of activation temperature since that K^+ is more active under higher temperature. Comparatively, the isotherm of MPC-9 is type I, reflecting its micropore characterization. PSDs of the prepared carbon materials are determined by N_2 and CO_2 sorption measurements. As shown apparently in the PSDs plots (Fig. 2b, c), all the carbon materials, except MPC-9, have quite similar pore size distribution composed of lots of micropores (< 2.0 nm) and large-mesopores in the size range from 20 to 40 nm. Narrow micropores peaked at 0.4, 0.6 and 0.8 nm are determined by CO_2 sorption measurement (Fig. 3d, S3d). PSDs obtained by DFT method are in good agreement with conclusions qualitatively derived from the above analysis of nitrogen isotherms.

In order to explain the forming of hierarchical porosity, we analyzed the specific surface area and porosity of the hydrothermal-treated xerogels and direct-dried xerogels. No any porosity and specific surface area is determined for the hydrothermal-treated xerogels. Comparatively, pore volume of 0.05 cm^3 g^{-1} and specific surface area of 30 m^2 g^{-1} are determined for the direct-dried xerogels prepared by using double KOH. The mesopores in the range of 2.5-5.0 nm are determined in the framework of direct-dried xerogles which will convert to the large mesopores of HPC-9d carbon (Fig. S5). The increase of pore size after carbonization may be due to the strong shrink of xerogel frameworks in the carbonization process. Further, we optimized the hierarchical porous carbon by using different KOH dosage. For comparison, we plotted all the sorption isotherms and PSD plots of HPC carbons prepared at 900 °C together (Fig. S6). A hysteresis loop varied with KOH dosage is exhibited, indicating that the mesoporosity of the four carbons is different. It could be visually observed that the mesoporosity increases as the KOH dosage increases (Table S1). The HPC-9h carbon possesses very small mesoporosity. Although the HPC-9t possesses the highest mesoporosity, its specific surface area and pore volume is slightly smaller than those of HPC-9d. That may be due to its less micropores (contributed more to the whole specific surface area) and less larger-sized mesopores (>10 nm, contributed more to the whole pore volume). In a word, the hierarchical porous carbons are prepared here, but their porosities vary with KOH dosage. We suspect that this may be related to structure of polymers. However, the exact reason is unclear for us, and the research will be continued. As shown in Table 1, the specific surface area and pore volume of the activated carbons gradually increase from 524 to 1549 m^2 g^{-1} and from 0.31 to 0.81 cm^3 g^{-1}, and the HPC-9d prepared by using double molar amount of KOH shows the most developed porosity with the highest specific surface area and pore volume among all the prepared samples.

Together with the SEM and TEM observation, one can conclude that such HPC-*x* samples possess micro-/mesopore hierarchical system which is beneficial for the rapid diffusion kinetics of charged ions and MPC-9 possesses a pure narrow micropore texture. Hence, hierarchical porous or microporous carbon materials could be facilely obtained by pre-treating phenolic resin carboxylic acid salt hydrogels in different methods. It is worthy of noting that the HPC-*x* samples possess much abundant porosity, but the dosage of KOH (only 30 wt% of resins here) is much lower than the other KOH-activated carbons (usually 100-400 wt% of carbon precursor) [41]. The large surface areas of HPC-*x* are achieved by mono-dispersed K^+ ions as a form of $-COO^-K^+$ or $-O^-K^+$. The method employed in this work is one-step and template-free, all the process is facile and easy to handle, and can be reference to prepare other functional porous carbons.

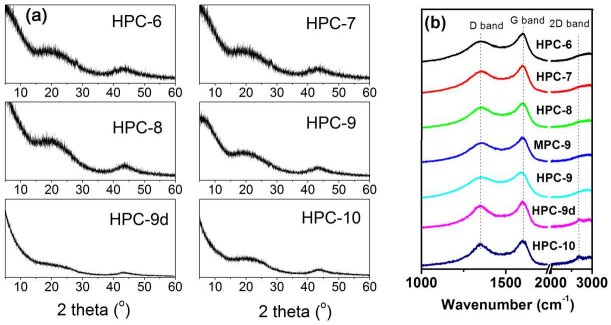

Fig. 4 - (a) XRD patterns and (b) Raman spectra of the samples

Fig. 4 shows the XRD patterns and Raman spectra of the prepared samples. As shown in Fig. 4a, no sharp peaks are present in their XRD patterns, demonstrating the characteristic of amorphous carbon resulted from the harsh K^+-activation. Two broad diffraction bands centred at 23.4° and 43° can be approximately indexed as (002) and (101) plane of graphite structure. Two major peaks centred at about 1589 and 1340 cm^{-1} are observed from Raman spectroscopy, usually called G band and D band, which are typical for disordered amorphous carbons [42, 43]. The G band corresponds to graphite in-plane vibrations with E_{2g} symmetry, but the D band was generally associated with breathing vibrations of sp^2 rings, characterising A_{1g} symmetry disallowed in graphite or the double-resonance Raman process in disordered carbon. An increase of the number of defects would result in an increase in the intensity of the D

peak and a concomitant drop in the intensity of the G peak. Thus, the larger I_D/I_G ratio is, the smaller graphite domain is obtained, resulting in the more defects. As shown in Table S2, the value of I_D/I_G roughly increased with the increasing of carbonization temperature, indicating that more defects are produced at higher carbonization temperature. That may be due to that the K^+ ions are more active at higher temperature. Obviously, 2D peak is observed for HPC-9d and HPC-10 indicating a graphitization occurs in some local regions of the carbon framework, which agrees well with the results of XRD and HRTEM observations (Fig. S3f).

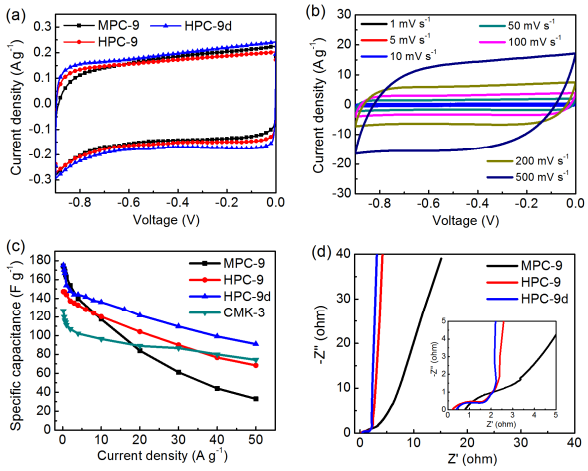

Fig. 5 - Electrochemical behavior of the prepared carbons in 6 M KOH electrolyte (a) cyclic voltammograms (CV) curves at 5 mV s^{-1}, (b) CV curves of HPC-9d at different scan rate, (c) specific capacitance at current densities in the range of 0.2-50 A g^{-1}, (d) Nyquist plots of the prepared carbons and enlarged Nyquist plots at high frequencies (inset)

The carbon materials of MPC-9, HPC-9 and HPC-9d are used as electrode materials of supercapacitor, and their capacitive performance are firstly studied in 6 M KOH electrolyte employing a standard two-electrode system (Fig. 5). As shown in Fig. 5a, standard rectangular-shaped CV curves are given by the investigated carbons, indicating a typical double layer capacitive nature of the charge/discharge process. CV curves of HPC-9d at scan rates between 1 and 500 mV s^{-1} are shown in Fig. 5c. This sample still maintains the appearance of roughly rectangular-like shapes at a very high scan rate, even up to 500 mV s^{-1}, indicating that this carbon has very good power performance. The good rate capability reflects that the ions of electrolyte could transfer fast and smoothly in the nano-channels of this carbon, which is due to the well-defined hierarchical porosity and short length of micropores.

In order to further investigated the capacitive performance of HPC-*x*, galvanostatic charge/discharge experiments were carried out at a large range of current density from 0.2-50 A g^{-1}. Standard isosceles triangle-like charge/discharge curves can be obtained at different current density, indicating excellent characteristic of reversible charge/discharge behavior and high coulombic efficiency (Fig. S7a). The low voltage drop at the initial of discharge branches indicates that the prepared carbon materials possess low resistances and good conductivities. The specific capacitance could be conveniently calculated by the galvanostatic discharge branches. At a current density of 0.2 A g^{-1}, the specific capacitance are determined to 174.4, 147.2 and 175.2 F g^{-1} for MPC-9, HPC-9 and HPC-9d, respectively. Although the specific surface area of MPC-9 is much lower than that of HPC-9 and HPC-9d, the specific capacitance of MPC-9 is similar to that of HPC-9d and higher than that of HPC-9 at 0.2 A g^{-1} in aqueous media. This may be due to the contribution of ultramicropores to the whole capacitance [44]. As shown in Fig. 3d, the MPC-9 carbon possesses much more ultramicropores (<0.5 nm) compared to HPC-9 and HPC-9d. Considering that the ion size of solvated K^+ and OH^- is about 0.35 nm in aqueous solution and the ion size of bare K^+ and OH^- is 0.27 and 0.28 nm, the ultramicropores could be accessible for the electrolyte ions at lower current density. In this contribution, the MPC-9 exhibits similar capacitance to HPC-9d, and much higher than that of HPC-9.

As shown in Fig. 5c, the specific capacitances of all the investigated carbons decrease with the increasing of charge/discharge current, which is a common feature of real supercapacitor since for the electrolyte ions there no enough time to diffusion into the entire pore surface, especially the narrow micropore surface, at higher charge current densities. However, HPC-9d still gives a high specific capacitance of 93.5 F g^{-1}, even when the current densities increased by 250 times, up to 50 A g^{-1}. The retention ratio of HPC-9d is calculated to be 53.4% in the range of 0.2~50 A g^{-1}, comparable to the CMK-3 carbon with 2-D hexagonal porosity (56.0% in the range of 0.2~50A g^{-1}). These good results further prove the advantage of the hierarchical porosity designed in this work. The tailored hierarchical pore texture with developed mesoporosity and short diffusion length makes ion transfer smoothly and conveniently and thus the electrolyte ions could reach to as much micropore surface as possible. It should be noted that the HPC-9d sample shows higher capacitance at all the current density measured. Specific volumetric capacitance is recently recommended to be a more reliable parameter than the gravimetric one to evaluate the real potential of a porous carbon for surpercapacitor applications. As shown in Fig. S7b, the HPC-9d sample gives a very high volumetric capacitance of 150.7 F cm^{-3} based on its high packing density (about 0.86 cm^3 g^{-1}), much higher than the CMK-3 carbon material (60 F cm^{-3}). The specific capacitances of HPC-9h and HPC-9t are also test in KOH electrolyte (Fig. S8). Due to the relatively low surface area, these two carbon exhibit lower specific capacitance than HPC-9d. It should be noted that the HPC-9t exhibits slight better rate capacity than HPC-9d because of its higher mesoporosity.

Nyquist plots of the activated carbons in a frequency range from 10 mHz to 100 kHz are also measured (Fig. 5d). The Nyquist plots are composed of four distinct parts, including an internal resistance when imaginary impedance is near to zero, an uncompleted semicircle at high frequency, a short 45° incline at middle frequency and a vertical line at low frequency, corresponding to ohmic resistances (R_s), charge transfer resistance (R_{ct}), Warburg impedance (W), and ideal double-layer capacitor, respectively. The very low value of R_s (<0.2 Ω) indicate the good conductivity of the test cell. The short lengths of Warburg slope and relative lower charge transfer resistance of HPC-9 and HPC-9d indicate that the electrolyte ions diffuse fast and electrons conduct well in the framework of these carbons, while the long slope of MPC-9 reflects that the ions move slowly in this carbon bulk due to its narrow microporosity. The Nyquist plots are further analysed using the following equation[45]:

$$C'(\omega) = -\frac{Z''(\omega)}{\omega|Z(\omega)|^2} \quad (4)$$

$$C''(\omega) = -\frac{Z'(\omega)}{\omega|Z(\omega)|^2} \quad (5)$$

$$\tau_0 = \frac{1}{\omega} = \frac{1}{2\pi f_0} \quad (6)$$

where $Z(\omega)$ is complex impedance, $Z'(\omega)$ is real impedance, $Z''(\omega)$ is imaginary impedance, $C'(\omega)$ is real capacitance, $C''(\omega)$ is imaginary capacitance, f_0 is a frequency corresponding to max value of $C''(\omega)$, and τ_0 is time relaxation constant. The relation plots of normalized $C'(\omega)$ and $C''(\omega)$ with frequency are illustrated in Fig. S9. It should be noted that the HPC-9d carbon still remain 50% of the saturated capacitance at a frequency of 5 Hz, while 40% and only 8% retention ratio are obtained for HPC-9 and MPC-9, indicating HPC-9d is promising for alternating current application. According to Equation (6), the relaxation time constants are determined to be 3.95, 0.36, 0.33 and 1.17s for MPC-9, HPC-9, HPC-9d and CMK-3, respectively (Fig. S4b, Table S3). The EIS results further confirm that these carbons are promising electrode materials for high power application.

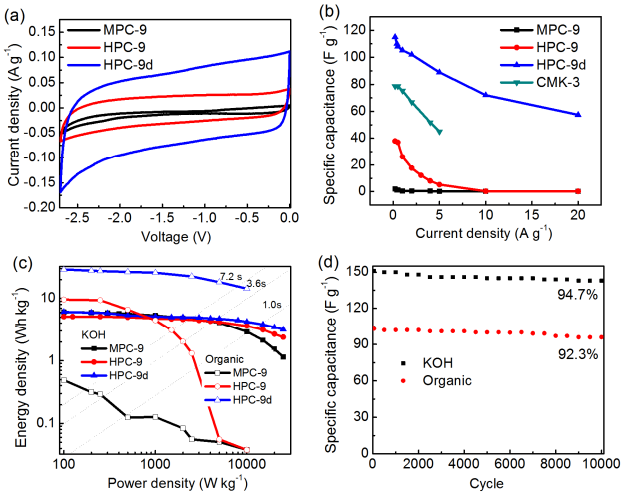

Fig. 6 Electrochemical behavior of the prepared carbons in 1 M $TEABF_4$/AN electrolyte (a) cyclic voltammograms (CV) curves at 10 mV s^{-1}, (b) specific capacitance at current densities in the range of 0.2-20 A g^{-1}, (c) Ragone plots of the prepared carbons, (d) long-term galvanostatic charge/discharge test of HPC-9d at 2 A g^{-1}

Considering the perfect conductivity and tailored hierarchical porosity, the electrochemical performance of the prepared carbons is also investigated in organic electrolyte of 1 M $TEABF_4$/AN electrolyte. As shown in Fig. 6a and S10, the standard rectangle-like CV curves and isosceles triangle-like charge/discharge curves prove the double layer capacitive behaviours of the investigated carbons. Apparently, the investigated carbons show distinct result in organic electrolyte with KOH electrolyte. Much lower current responses are given by MPC-9 indicating that this carbon has very low specific capacitance in organic electrolyte. This fact could be more evidently observed from Fig. 6b. Only 1.9 F g^{-1} is given by MPC-9. Comparatively, HPC-9d gives a high specific capacitance of 115 F g^{-1} at 0.2 A g^{-1}, and still remains 57.5 F g^{-1} at 20 A g^{-1}, indicating that this carbon possess much higher accessible pore space. Such an evident distinction may be contributed to PSDs of the investigated carbons. Only the pores larger than 0.7 nm is effective for double-layer accumulation under the TEABF4/AN system (size: solvated and unsolvated TEA^+ of 1.3 and 0.67 nm; solvated and unsolvated BF_4^- of 1.16 and 0.48 nm, respectively). As shown in Fig. 3d, large amount of ultramicropores (0.7-1.0 nm) of HPC-9d gives a large effective specific surface area for forming electric double-layer, thus affording a high capacitance. Comparatively, the most micropores of HPC-9 are smaller than 0.7 nm which are too small to be accessible for ions of organic electrolyte. We calculated the specific surface area for the pore larger than 0.7 nm, which is 777 m^2 g^{-1} and 340 m^2 g^{-1} for HPC-9d and HPC-9, respectively. We believed that this difference in the specific surface area (>0.7 nm) attributed to the large distinction of specific capacitance. Further considering the ion diffusion in a short charge/discharge time (at higher current density) and the solvation of electrolyte ions, larger micropores and mesopores are needed. Thus, the HPC-9 carbon shows very small specific capacitance under high current densities (> 10 A g^{-1}).

Ragone plots are displayed in Fig. 6c. It could be seen that all the Ragone plots gradually slope down as power density increases, which means that less energy can be released at higher power output. The supercapacitors using organic electrolyte deliver much higher energy density than those using KOH electrolyte since the energy density is proportion to the square of cell voltage. Remarkable energy densities of 29.1 and 6.1 Wh kg^{-1} are delivered by HPC-9d in organic and KOH electrolyte, respectively. The energy and power density of HPC-9d are 14.4 Wh kg^{-1} and 10 000 W kg^{-1} in organic electrolyte at a current drain time of 3.6 s, and are 4.0 Wh kg^{-1} and 15 000 W kg^{-1} at a very short current drain time of 1.0 s in KOH electrolyte, both being highest among the investigated materials. The maximum power density P_{max} for HPC-9d in both electrolytes could be calculated according to Equation 7[46, 47]:

$$P_{max} = \frac{V^2}{4ESR \cdot \omega} \quad (7)$$

where ESR is the equivalent series resistance obtained from Nyquist plots at f = 1 kHz, and ω is the total active material weight of supercapacitor. Very high maximum power densities are obtained, that is 113 and 300 kW kg^{-1} for KOH and organic electrolyte, respectively, further testifying the high power capability of HPC-9d.

Finally, the long-term cyclic stability of HPC-9d in both electrolytes are measured by using galvanostatic charge/discharge test up to 10 000 cycles at 2 A g^{-1} (Fig. 6d). The capacitance of HPC-9d gradually decreases during this period which is a common phenomenon in real application. After 10 000 cycles, this carbon shows an excellent characteristic of recycling charge/discharge performance with a high retention ratio of 94.7% and 92.3% based on the discharge capacitance of the initial cycle in KOH and organic electrolyte, respectively.

Conclusions

A template-free and one-step method is developed to prepare hierarchical porous carbon materials, that is direct carbonization of phenolic resin carboxylic salt xerogels. A microporous carbon material with narrow pore size distribution is also facilely prepared by hydrothermal-treated resin hydrogels. The HPC-*x* samples possess typical hierarchical porosity simultaneous possessing interconnected mesopores and developed micropores with very short length. Due to its unique pore texture, the HPC-9d carbon shows superior capacitive performance with high specific capacitance, excellent rate capability, and good long-term cycle stability in KOH and $TEABF_4$/AN electrolyte. In a word, the method employed in this work is facile and easy to handle, and the prepared carbon materials are promising for supercapacitors combined high energy density and high power output.

Acknowledgment

This work was financially supported by Natural Science Foundation of China (NSFC 51302156) and Young Teacher Supporting Fund of Shandong University of Technology.

Supporting Informations. Photographic pictures of the hydrogel and xerogel, SEM and TEM images of HPC-6, HPC-7, HPC-8, HPC-9 and HPC-10, nitrogen sorption isotherms, NLDFT pore size distribution of HPC-x, Galvanostatic charge/discharge curves at different current density, volumetric capacitance of HPC-9d and CMK-3 in KOH and organic electrolytes, normalized imaginary capacitance vs. alternative current frequency, CV and galvanostatic charge/discharge curves of HPC-9d in TEABF4/AN electrolyte, Values of ID/IG, Specific capacitance at 0.20 A g-1 and the time constant in KOH electrolyte.

Notes and references

School of Chemical Engineering,

Shandong University of Technology,

Zibo 255049, P. R. China.

Tel. /fax: +86 533 2781664

**Corresponding author: Jin Zhou*

Email:zhoujsdut@gmail.com

**Corresponding author: Shuping Zhuo*

E-mails: zhuosp_academic@yahoo.com

†These authors contributed equally to this work.

References

1. P. Simon and Y. Gogotsi, *Nature Materials*, 2008, **7**, 845-854.
2. A. L. Reddy, S. R. Gowda, M. M. Shaijumon and P. M. Ajayan, *Advanced materials*, 2012, **24**, 5045-5064.
3. Y. Zhu, S. Murali, M. D. Stoller, K. J. Ganesh, W. Cai, P. J. Ferreira, A. Pirkle, R. M. Wallace, K. A. Cychosz, M. Thommes, D. Su, E. A. Stach and R. S. Ruoff, *Science*, 2011, **332**, 1537-1541.
4. T. Kim, G. Jung, S. Yoo, K. S. Suh and R. S. Ruoff, *ACS nano*, 2013, **7**, 6899-6905.
5. L. Nyholm, G. Nystrom, A. Mihranyan and M. Stromme, *Advanced materials*, 2011, **23**, 3751-3769.
6. H.-P. Cong, X.-C. Ren, P. Wang and S.-H. Yu, *Energy & Environmental Science*, 2013, **6**, 1185.
7. C. Mondal, M. Ganguly, P. K. Manna, S. Yusuf and T. Pal, *Langmuir*, 2013, **29**, 9179-9187.
8. N. Kang, T. Yu, G.-H. Lim, T. Koh and B. Lim, *Chemical Physics Letters*, 2014, **592**, 192-195.
9. H. Chen, L. Hu, M. Chen, Y. Yan and L. Wu, *Advanced Functional Materials*, 2014, **24**, 934-942.
10. A. Ghosh and Y. H. Lee, *ChemSusChem*, 2012, **5**, 480-499.
11. L. Dai, D. W. Chang, J. B. Baek and W. Lu, *Small*, 2012, **8**, 1130-1166.
12. L. Wei and G. Yushin, *Nano Energy*, 2012, **1**, 552-565.
13. Y. Zhai, Y. Dou, D. Zhao, P. F. Fulvio, R. T. Mayes and S. Dai, *Advanced materials*, 2011, **23**, 4828-4850.
14. X. Fang, J. Zang, X. Wang, M.-S. Zheng and N. Zheng, *Journal of Materials Chemistry A*, 2014, **2**, 6191-6197.
15. H. Ji, X. Zhao, Z. Qiao, J. Jung, Y. Zhu, Y. Lu, L. L. Zhang, A. H. MacDonald and R. S. Ruoff, *Nature communications*, 2014, **5**.
16. J. Chmiola, G. Yushin, Y. Gogotsi, C. Portet, P. Simon and P. L. Taberna, *Science*, 2006, **313**, 1760-1763.
17. C. Largeot, C. Portet, J. Chmiola, P.-L. Taberna, Y. Gogotsi and P. Simon, *Journal of the American Chemical Society*, 2008, **130**, 2730-2731.
18. C. Merlet, B. Rotenberg, P. A. Madden, P.-L. Taberna, P. Simon, Y. Gogotsi and M. Salanne, *Nature materials*, 2012, **11**, 306-310.
19. W. Xing, S. Z. Qiao, R. G. Ding, F. Li, G. Q. Lu, Z. F. Yan and H. M. Cheng, *Carbon*, 2006, **44**, 216-224.
20. D.-W. Wang, F. Li, M. Liu, G. Lu and H.-M. Cheng, *Angewandte Chemie International Edition*, 2008, **47**, 373-376.
21. H.-J. Liu, X.-M. Wang, W.-J. Cui, Y.-Q. Dou, D.-Y. Zhao and Y.-Y. Xia, *Journal of Materials Chemistry*, 2010, **20**, 4223-4230.
22. W. Li, F. Zhang, Y. Dou, Z. Wu, H. Liu, X. Qian, D. Gu, Y. Xia, B. Tu and D. Zhao, *Advanced Energy Materials*, 2011, **1**, 382-386.
23. C. H. Huang, Q. Zhang, T. C. Chou, C. M. Chen, D. S. Su and R. A. Doong, *ChemSusChem*, 2012, **5**, 563-571.
24. W. Huang, H. Zhang, Y. Huang, W. Wang and S. Wei, *Carbon*, 2011, **49**, 838-843.
25. W. Xing, C. C. Huang, S. P. Zhuo, X. Yuan, G. Q. Wang, D. Hulicova-Jurcakova, Z. F. Yan and G. Q. Lu, *Carbon*, 2009, **47**, 1715-1722.
26. K. Xia, Q. Gao, J. Jiang and J. Hu, *Carbon*, 2008, **46**, 1718-1726.
27. Z. Zheng and Q. Gao, *Journal of Power Sources*, 2011, **196**, 1615-1619.
28. Y. Han, X. Dong, C. Zhang and S. Liu, *Journal of Power Sources*, 2013, **227**, 118-122.
29. X. He, N. Zhao, J. Qiu, N. Xiao, M. Yu, C. Yu, X. Zhang and M. Zheng, *Journal of Materials Chemistry A*, 2013, **1**, 9440-9448.
30. R.-w. Fu, Z.-h. Li, Y.-r. Liang, F. Li, F. Xu and D.-c. Wu, *New Carbon Materials*, 2011, **26**, 171-179.
31. Y. Han, X. Dong, C. Zhang and S. Liu, *Journal of Power Sources*, 2012, **211**, 92-96.
32. Q. Wang, J. Yan, Y. Wang, T. Wei, M. Zhang, X. Jing and Z. Fan, *Carbon*, 2014, **67**, 119-127.
33. L. Estevez, R. Dua, N. Bhandari, A. Ramanujapuram, P. Wang and E. P. Giannelis, *Energy & Environmental Science*, 2013, **6**, 1785-1790.

34. J. Zhang, L. Jin, J. Cheng and H. Hu, *Carbon*, 2013, **55**, 221-232.
35. A. Taguchi, J. H. Smått and M. Lindén, *Advanced Materials*, 2003, **15**, 1209-1211.
36. Y. Lv, F. Zhang, Y. Dou, Y. Zhai, J. Wang, H. Liu, Y. Xia, B. Tu and D. Zhao, *Journal of Materials Chemistry*, 2012, **22**, 93-99.
37. D.-C. Guo, J. Mi, G.-P. Hao, W. Dong, G. Xiong, W.-C. Li and A.-H. Lu, *Energy & Environmental Science*, 2013, **6**, 652-659.
38. T.-c. Chou, C.-h. Huang, R.-a. Doong and C.-c. Hu, *Journal of Materials Chemistry A*, 2013, **1**, 2886-2895.
39. J. Liang, X. Du, C. Gibson, X. W. Du and S. Z. Qiao, *Advanced Materials*, 2013, **25**, 6226-6231.
40. S. Jun, S. H. Joo, R. Ryoo, M. Kruk, M. Jaroniec, Z. Liu, T. Ohsuna and O. Terasaki, *Journal of the American Chemical Society*, 2000, **122**, 10712-10713.
41. J. Wang and S. Kaskel, *Journal of Materials Chemistry*, 2012, **22**, 23710-23725.
42. S.-H. Park, S.-M. Bak, K.-H. Kim, J.-P. Jegal, S.-I. Lee, J. Lee and K.-B. Kim, *Journal of Materials Chemistry*, 2011, **21**, 680-686.
43. C.-Y. Su, Y. Xu, W. Zhang, J. Zhao, X. Tang, C.-H. Tsai and L.-J. Li, *Chemistry of Materials*, 2009, **21**, 5674-5680.
44. X. Wu, W. Xing, J. Florek, J. Zhou, G. Wang, S. Zhuo, Q. Xue, Z. Yan and F. Kleitz, *Journal of Materials Chemistry A*, 2014, **2**, 18998-19004.
45. P. Taberna, P. Simon and J.-F. Fauvarque, *Journal of The Electrochemical Society*, 2003, **150**, A292-A300.
46. Y. Wang, Z. Shi, Y. Huang, Y. Ma, C. Wang, M. Chen and Y. Chen, *The Journal of Physical Chemistry C*, 2009, **113**, 13103-13107.
47. C. Du, J. Yeh and N. Pan, *Nanotechnology*, 2005, **16**, 350-353.

